Hot-electron preheat and mitigation in polar-direct-drive experiments at the National Ignition Facility

A. A. Solodov,[1,*] M. J. Rosenberg,[1] M. Stoeckl,[1] A. R. Christopherson,[2] R. Betti,[1] P. B. Radha,[1] C. Stoeckl,[1] M. Hohenberger,[2] B. Bachmann,[2] R. Epstein,[1] R. K. Follett,[1] W. Seka,[1] J. F. Myatt,[3] P. Michel,[2] S. P. Regan,[1] J. P. Palastro,[1] D. H. Froula,[1] E. M. Campbell,[1] and V. N. Goncharov[1]

[1]*Laboratory for Laser Energetics, University of Rochester, Rochester, New York 14627, USA*

[2]*Lawrence Livermore National Laboratory, Livermore, California 94550, USA*

[3]*Department of Electrical and Computer Engineering, University of Alberta, Edmonton T6G 2R3, Canada*

(Received 14 October 2021; revised 18 April 2022; accepted 14 October 2022; published 4 November 2022)

Target preheat by superthermal electrons from laser-plasma instabilities is a major obstacle to achieving thermonuclear ignition via direct-drive inertial confinement fusion at the National Ignition Facility (NIF). Polar-direct-drive surrogate plastic implosion experiments were performed on the NIF to quantify preheat levels at an ignition-relevant scale and develop mitigation strategies. The experiments were used to infer the hot-electron temperature, energy fraction, and divergence, and to directly measure the spatial hot-electron energy deposition profile inside the imploding shell. Silicon layers buried in the ablator are shown to mitigate the growth of laser-plasma instabilities and reduce preheat, providing a promising path forward for ignition designs at an on-target intensity of about 10^{15} W/cm^2.

DOI: 10.1103/PhysRevE.106.055204

I. INTRODUCTION

In direct-drive inertial confinement fusion (ICF) [1,2] a capsule containing cryogenic deuterium-tritium (DT) fusion fuel surrounded by an ablator such as plastic (CH) is irradiated by multiple laser beams. The beams ablate the outer material, driving the implosion via the rocket effect, and compress the cryogenic DT to fusion conditions. For efficient implosion and compression, the thermonuclear fuel must be kept at low entropy. The shell entropy is measured by the adiabat, defined as the ratio of the DT pressure to the Fermi-degenerate pressure. Preheat by suprathermal electrons generated by laser-plasma instabilities (LPIs) raises the adiabat, degrades the implosion, and prevents ignition.

The direct-drive approach to laser fusion [2] is susceptible to hot-electron preheat due to the long-scale-length plasma conditions near the quarter-critical density $n_c/4$ [where $n_c \approx 1.1 \times 10^{21}\lambda_0^{-2}$ cm^{-3} is the critical density and λ_0 (in μm) is the laser wavelength]. Parametric instabilities such as stimulated Raman scattering (SRS) [3–5] develop for direct-drive laser intensities in such plasmas, generating plasma waves capable of trapping and accelerating electrons to superthermal energies.

Recent experiments at the National Ignition Facility (NIF) [6] using planar targets demonstrated [7–9] that at direct-drive ignition-relevant plasma conditions, SRS is the dominant hot-electron source. This is unlike prior experiments on OMEGA at shorter plasma density scale lengths and lower temperatures, where the dominant instability was two-plasmon decay (TPD) [10–14].

Layers of mid-Z materials, such as silicon, strategically placed in the ablators were previously shown to mitigate TPD in OMEGA implosions [15]. Planar experiments on the NIF demonstrated that mid-Z materials are effective in mitigating SRS and hot-electron production at direct-drive ignition-relevant conditions [7,8]. SRS is mitigated [5,16] by shortening the density scale length and by increasing the electron-ion collisional rate ($\nu_{ei} \propto Z_{eff} = \langle Z^2\rangle/\langle Z\rangle$, where Z is the ion charge state). Higher collisionality enhances the absorption of the incident and scattered light, and damps electron plasma waves.

While NIF planar experiments identified SRS as the dominant instability, it is critical for the viability of direct drive to quantify hot-electron production in spherical geometry, the divergence of the hot-electron source, the hot-electron coupling to the imploding shell, and the spatial distribution of preheat energy. In ICF, the inertial confinement of the hot-spot pressure is provided by the shell mass that stagnates at the time of peak neutron production (bang time). The stagnating mass is enclosed by the outgoing rebound shock driven by the hot-spot pressure and provides most of the core areal density. If preheated while in flight, this inner shell region cannot assemble the areal densities required for ignition. Therefore, it is crucial to measure the spatial distribution of the preheat energy within the shell while in flight. Knowledge of the laser to hot-electron conversion efficiency is insufficient for assessing preheat since most hot electrons deposit their energy in the ablated plasma rather than inside the shell.

II. EXPERIMENT AND METHOD OF ANALYSIS

In this paper, we present measurements of the hot-electron energy deposition in NIF-scale implosions. Surrogate fuel

*asol@lle.rochester.edu

 ©2022 American Physical Society

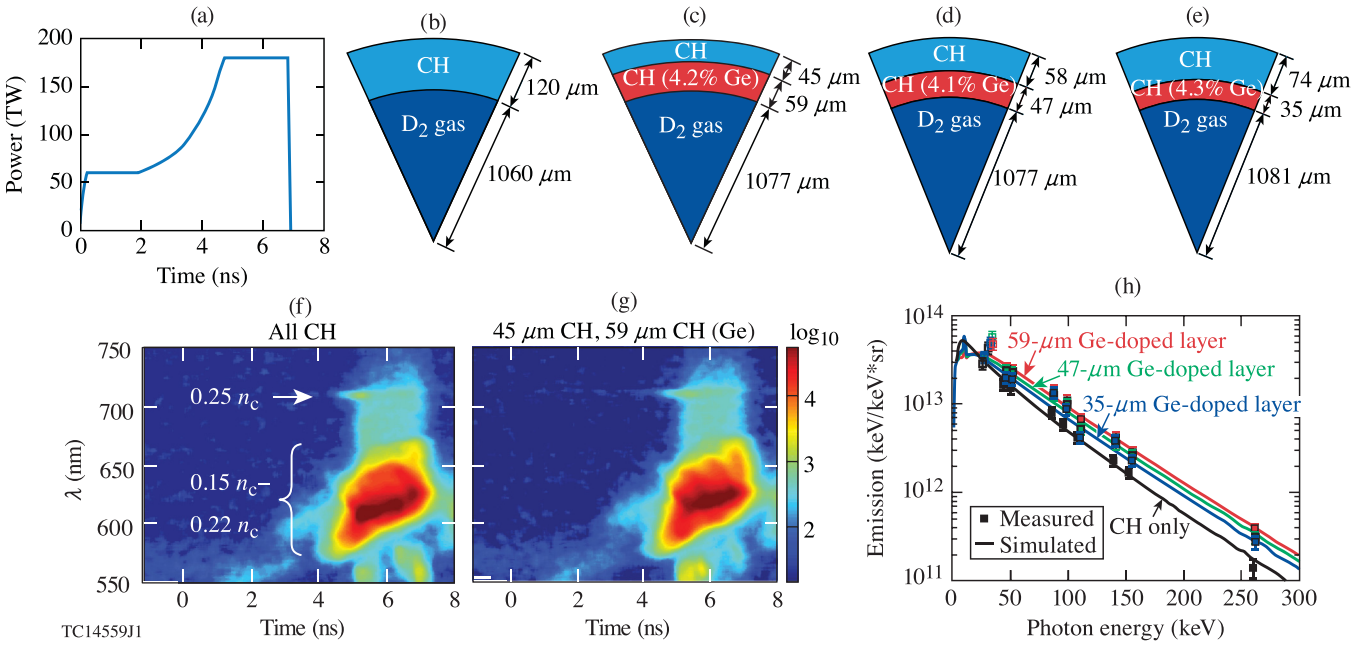

FIG. 1. (a) The total laser power profile. (b)–(e) Design of the targets having CH ablators. Different thicknesses of the Ge-doped layer in the multilayered targets (c)–(e) were used to establish the hot-electron energy deposition profile in the unablated shell. (f), (g) Time-resolved scattered-light spectra at a collection angle of 23.5° relative to the NIF south pole, obtained in the experiments for targets (b) and (c). LPI is dominated by SRS at $n_c/4$ and lower densities and is almost identical in the two shots. (h) Measured and simulated time-integrated HXR spectra.

capsules are driven by a shaped 351-nm laser pulse with a total energy of 720 kJ [Figs. 1(a)–1(e)] in the polar-direct-drive (PDD) NIF geometry [17], proposed to accommodate direct-drive experiments using the current indirect (x-ray) drive NIF beam configuration. The experiments use ∼2.4-mm-diameter capsules, chosen to match the size of the indirect-drive phase plates. They are only ∼30% smaller than the targets in the proposed ignition NIF PDD design [18].

In the PDD geometry, NIF beams arranged in cones at 23.5°–50° from the poles are repointed increasingly toward the equator the further they are located from the poles, as the equator requires additional drive for symmetric target irradiation. The combination of beam displacements, beam defocus, and beam pulse shapes had been adjusted to improve the shell irradiation symmetry, as described in Ref. [19].

The hot-electron radial energy deposition profile is inferred by employing mass-equivalent plastic targets with inner Ge-doped layers and comparing the measured hard x-ray (HXR) spectra to simulations. The thickness of the Ge-doped (at ∼4% atomic percent) layer was varied to establish the hot-electron energy deposition profile in the unablated shell. Coupling of ∼0.2% of the laser energy to the inner 80% of the unablated shell is inferred at the incident laser intensity of 10^{15} W/cm^2. This is close to ∼0.15% of the laser energy, which is thought to be acceptable in the present direct-drive ignition designs [20].

It is also shown that a buried thin mid-Z Si layer strongly mitigates SRS and hot-electron preheat. The Si layer was designed to be ablated to pass through the $n_c/4$ region during the most intense part of the laser pulse. Preheat reduction by a factor of ∼2 demonstrates that this promising preheat-mitigation strategy can expand the ignition-design space to higher intensity.

In the targets with CH ablators, the thicknesses of the Ge-doped layer were varied from 35 to 59 μm [Figs. 1(c)–1(e)] and the HXR emission was compared to the HXR emission from the reference all-CH target [Fig. 1(b)]. The HXR emission was measured using the 10-channel NIF filter-fluorescer x-ray (FFLEX) diagnostic [21].

The multilayered target platform to study hot-electron preheat and energy deposition was suggested by Christopherson *et al.* [22] on the OMEGA laser, using plastic targets with inner cryo-DT and Cu-doped layers. A formula was derived for the preheat energy deposition in the inner layer proportional to the difference of the HXR emission between implosions with all-CH and with a different payload material. A uniform preheat energy deposition in the unablated shell was inferred in OMEGA experiments, where the mean hot-electron range significantly exceeded the shell areal density (ρR). The targets in the NIF experiments are larger and thicker and the energy deposition is no longer uniform. Targets with inner Ge-doped layers are opaque to x rays with energy below ∼40 keV, so that not all the emission escapes and reaches FFLEX. The spectrum of hot electrons evolves as they penetrate through the target and multiple scattering results in electrons escaping from the target before they deposit all their energy. These effects are not accounted for by the simple preheat formula and necessitate detailed Monte Carlo simulations of the hot-electron transport in the imploded plasma to analyze the preheat.

NIF target implosions were simulated using the one-dimensional (1D) hydrodynamic code LILAC [23]. Similar

all-CH implosions were previously simulated [19] using the 2D hydrocode DRACO [24]. The simulations predict similar coronal conditions for all of the mass-equivalent targets shown in Figs. 1(b)–1(e), with the density scale length at the $n_c/4$ surface of 420 μm, an electron temperature of 3.5 keV, and an overlapped intensity of 4.5×10^{14} W/cm^2. Similar coronal conditions indicate that similar LPIs and hot-electron generation can be expected. Indeed, the measured scattered-light spectra were almost identical in the experiments. SRS spectra for the targets in Figs. 1(b) and 1(c) are shown in Figs. 1(f) and 1(g). As in the NIF planar experiments [7,9], the spectra show an absolute SRS signature from $n_c/4$ and a lower-density (∼0.15 to 0.22 n_c) SRS feature [25]. The Monte Carlo code GEANT4 [26] modeled hot-electron transport, energy deposition, and bremsstrahlung emission in the imploding shell using the plasma profiles from LILAC simulations during the most intense flat-top part of the laser pulse when the majority of the hot electrons were generated.

In the GEANT4 simulations, hot electrons were injected at the $n_c/4$ surface with a Maxwellian energy distribution and the temperature (T_{hot}), total energy, and divergence half angle ($\theta_{1/2}$) were varied to best match the measured HXR spectra. $\theta_{1/2}$ is found to exceed the half angle at which the dense shell is seen from the $n_c/4$ surface during the implosion, $\theta_{1/2} > \theta_{sh} \approx 40°$–$45°$. To match the HXR spectra for all the mass-equivalent implosions, a fraction of the HXR emission should be generated by hot electrons recirculating in the outer CH corona. This fraction represents $34 \pm 10\%$ to $10 \pm 10\%$ of the emission in all-CH target for $\theta_{1/2}$ increasing from 45° to 135°. Hot-electron refluxing was not modeled explicitly because a detailed theory of refluxing does not exist [27]. A fraction of the HXR spectrum for the all-CH target was used to approximate the HXR emission from recirculating electrons and was subtracted from all the measured spectra. Although $\theta_{1/2}$ and, consequently, the total energy of generated electrons are not fully constrained, the hot-electron energy deposition in the imploded shell (preheat) is well constrained. The inferred hot-electron energy deposition in the Ge-doped layers of the multilayered targets (and, consequently, in the entire unablated shell) is independent of $\theta_{1/2}$ (exceeding θ_{sh}) and it depends only on the difference of the HXR emission in the experiments with and without Ge-doped layers.

III. RESULTS

The HXR spectra measured in the experiments and their best fits using the simulated spectra at $\theta_{1/2} = 90°$ are shown in Fig. 1(h). The inferred hot-electron temperature $T_{hot} = 56 \pm 2$ keV. The hot-electron energy deposition profile for the all-CH target, based on the simulation that best fit the data, is plotted in Fig. 2. Figure 2(a) shows the cumulative hot-electron energy fraction in percent of the laser energy ($E_L = 720$ kJ) and Fig. 2(b) shows the preheat density in kJ/mg. They are plotted as functions of the radial coordinate in the unimploded shell, measured from the inner shell radius (playing the role of the Lagrangian coordinate of the radial mass elements in the imploding shell). The insets show the energy deposition in the unablated part of the shell in more detail. The red circles in Fig. 2(a) show the hot-electron energy depositions in the Ge-doped layers in the simulations of the multilayered targets

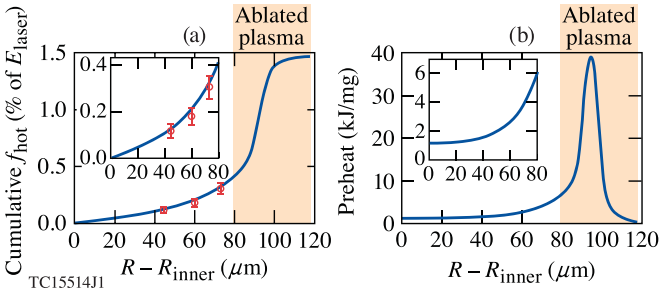

FIG. 2. (a) The cumulative hot-electron energy fraction and (b) the preheat density in the simulation for the all-CH target shown in Fig. 1(b) plotted as functions of the radial coordinate in the unimploded shell, measured from the inner shell radius. The insets show the energy deposition in the unablated part of the shell in more detail. The red circles show the inferred hot-electron energy depositions in the Ge-doped layers of the multilayered targets shown in Figs. 1(c)–1(e).

plotted versus the mass-equivalent radius (or thickness) in the all-CH target. The inferred energy depositions in the multilayered and all-CH targets are in good agreement. The values of the error bars shown for the multilayered targets (resulting from the statistical uncertainties of the HXR spectral fits) also represent well the error bars for the all-CH target.

The simulations that best fit the experimental HXR data were determined by minimizing the total χ^2 difference between the measured and simulated FFLEX channel signals. The dominant sources of error were the statistical uncertainties of ∼15% in the FFLEX channel signals. FFLEX channels 3 to 10 were used in the fitting procedure (5 to 10 in the experiments with a Si layer below) because the lower energy channels were affected by the coronal thermal x-ray emission. While some of the FFLEX channels, such as channel 7 at around 110 keV, showed systematically lower or higher signals in all the shots (probably because of a calibration error), this did not much affect the fitting error because these variations were usually within the statistical error bars. The error bars for the fitting parameters (hot-electron temperature, energy, and energy deposited by recirculating electrons) correspond to the confidence regions near the minimum of χ^2 with the confidence level of 68%, that is, one standard deviation.

Figure 2 demonstrates that most of the hot-electron energy is deposited in the plasma which is ablated during the implosion. This includes ∼1.05% of E_L according to Fig. 2(a), plus ∼0.35% of E_L deposited by recirculating electrons in the outer corona (which generate an additional ∼18% of the HXR emission at $\theta_{1/2} = 90°$). The energy deposited in the unablated shell ($R - R_{inner} < 79.5$ μm) is $0.4 \pm 0.08\%$ of E_L or ∼22% of the total deposited energy. Importantly, the energy deposition in the unablated shell peaks at its outer edge with only about half of the energy deposited in the inner 80% of the unablated shell. The energy deposition decreases toward the shell center because of the electron collisional slowing down and stopping in the outer CH.

The total hot-electron energy deposition in the unablated shell exceeds 0.15% of the laser energy, which is estimated as the maximum tolerable hot-electron preheat in present direct-drive implosions designed for ignition and high gain [20].

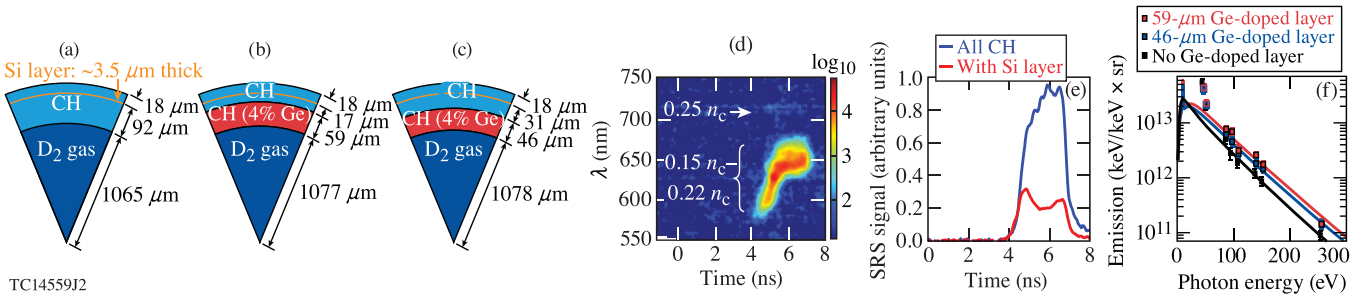

FIG. 3. (a)–(c) Targets having a Si layer in the ablator. Different thicknesses of the Ge-doped layer in the targets (b),(c) were used to establish the hot-electron energy deposition profile in the unablated shell. (d) Time-resolved scattered-light spectrum at collection angle of 23.5° relative to the NIF south pole in the experiment for targets (a). (e) Time-resolved SRS scattered-light energy averaged over the collection angles of 30° and 50° (obtained using the full aperture backscatter stations [28]) in implosions of CH targets with and without a Si layer [Figs. 1(b) and 3(a)]. SRS is significantly reduced when Si reaches the $n_c/4$ region at the beginning of the laser flat-top in the implosion with a Si layer. (f) Measured and simulated time-integrated HXR spectra.

In the following, we demonstrate that thin layers of mid-Z material, such as Si, strategically placed in the ablator, mitigate SRS and reduce hot-electron preheat to an acceptable level.

Figures 3(a)–3(c) show the mass-equivalent targets having a buried Si layer, designed to pass through the $n_c/4$ region during the laser flat-top. Time-resolved SRS spectrum [Fig. 3(d)] and scattered-light energy [Fig. 3(e)] show a significant reduction of SRS compared to the experiment without a Si layer. Similar to the implosions without a Si layer, a wide divergence half angle of hot electrons $\theta_{1/2} > \theta_{sh}$ is inferred. Figure 3(f) shows the measured HXR spectra and their best fits using the simulated spectra at $\theta_{1/2} = 90°$, at which 5±15% of the HXR energy is attributed to recirculating electrons in the implosion without a Ge-doped layer. The inferred hot-electron temperature $T_{hot} = 52 \pm 2$ keV. Hot-electron energy deposition in the CH target with a Si layer [Fig. 3(a)] is plotted in Fig. 4, with red circles showing the energy depositions in the Ge-doped layers of the targets in Figs. 3(b) and 3(c). As in the all-CH target, a significant fraction of the deposited energy, ~75%, is in the ablated plasma, and ~25% in the unablated shell. About 0.22% of the total laser energy is deposited in the unablated shell, with half of it in the inner 80% of the unablated shell. For a comparison, the energy depositions in the Ge-doped layers in the experiments without a Si layer are shown in Fig. 4(a) by purple circles. With a Si layer, hot-electron energy deposition in the unablated shell reduces by about a factor of 2, which demonstrates an important mitigation effect. Hot-electron preheat reduction is consistent across all three experiments using Si layers, showing a good reproducibility.

Hot-electron preheat in the targets without a Si layer was also studied at a 25% reduced flat-top laser power and intensity. Figure 5 summarizes the hot-electron energy deposition in the unablated shell inferred in our experiments. The preheat of 0.4% at the incident laser intensity of 10^{15} W/cm^2 (without a Si layer) is reduced by about a factor of 2 for laser intensity of 0.75×10^{15} W/cm^2. A similar preheat reduction is achieved at 10^{15} W/cm^2 using a Si layer in the ablator. Preheat reduction by a factor of 2 or more using a Si ablator was previously obtained in NIF planar experiments [8] over a wide range of intensities relevant to direct-drive ICF. The experiments reported here are an important confirmation that Si is effective as a layer in spherical implosions.

Though a mid-Z layer reduces hot-electron preheat, its effect on implosion hydrodynamics must be considered [29].

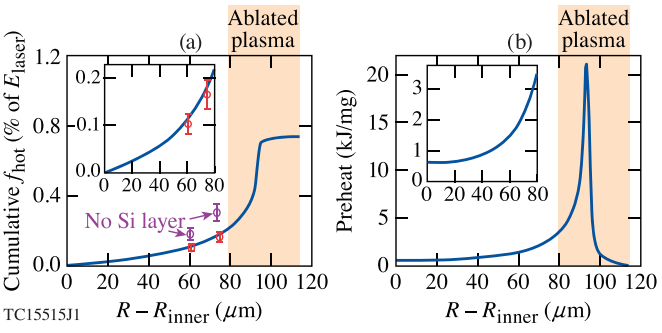

FIG. 4. (a) The cumulative hot-electron energy fraction and (b) the preheat density in the simulation for the target with a Si layer shown in Fig. 3(a) plotted as functions of the radial coordinate in the unimploded shell, measured from the inner shell radius. The insets show the energy deposition in the unablated part of the shell in more detail. The red (purple) circles show the inferred hot-electron energy depositions in the Ge-doped layers of the targets shown in Figs. 3(b) and 3(c) [Figs. 1(c) and 1(d)].

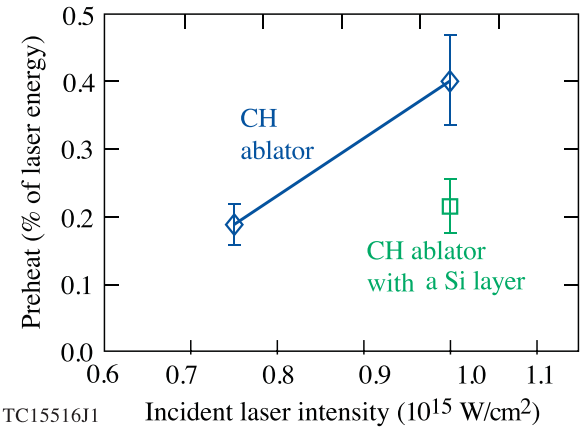

FIG. 5. Hot-electron preheat inferred in the experiments using targets with a CH ablator (at two incident intensities) and a Si layer in the ablator.

While a mid-Z layer usefully increases the laser inverse-bremsstrahlung absorption and reduces cross-beam energy transfer, it lowers the hydrodynamic efficiency and increases the radiative preheat of the shell. It has been recommended [29] to keep the mid-Z layer thin and place it inside the lower-Z material to combine the higher laser absorption with the larger ablation efficiency of the innermost layer in the ablator. Note that the implosion trajectory data obtained using soft x-ray self-emission in the present experiments showed similar implosion velocities between the experiments with and without a Si layer in the ablator, without loss of the implosion efficiency. Although more work is required to assess the stability properties of the multilayer designs, Si expansion caused by absorption of the coronal radiation reduces its density and Atwood number at the outer Si/CH interface, helping to mitigate Rayleigh-Taylor instability.

These results from warm, subscale implosions can be extrapolated to estimate preheat in the future cryogenic DT, ignition-scale PDD implosions. Based on the present experiments, preheat into the inner 80% of the unablated shell is ∼0.2% of the laser energy at an intensity of 10^{15} W/cm^2. Comparison of the total hot-electron energy coupled to the plasma in the present experiment (∼1.8%) and hydrodynamically equivalent implosions on OMEGA (scaled down by a factor of 3.4 in size and 40 in energy) [30] indicates that the fraction of laser energy coupled to hot electrons scales proportionally to the target size. With an increase by ∼1.4 in size from subscale to ignition-scale implosions, we estimate a similar increase in the hot-electron energy fraction and preheat. An upper limit for the hot-electron energy coupling of ∼4% was obtained in planar NIF experiments at direct-drive ignition-relevant conditions [8] (at the similar single-beam intensity and beam overlap). Ignition design implosions are faster and have a larger shell convergence ratio during the peak hot-electron production: 2–3 instead of 1.5–2 in the present experiments. Given a large hot-electron divergence inferred in the present experiments, the preheat will be reduced by the ratio of the solid angles at which the dense core is seen from the $n_c/4$ region, that is, ∼1–2. A reduced hot-electron attenuation in the ablated and compressed-shell DT in ignition implosions [18,31], relative to warm implosions with CH ablators, has been verified using LILAC and GEANT4 simulations with the hot-electron source inferred in the present experiments. A more-uniform hot-electron energy deposition across the radius results in an ∼2× higher preheat density in the inner 50% of the unablated shell, while the total preheat in the inner ∼80% of the unablated shell is nearly unchanged.

Combining all these factors results in an estimated preheat of ∼0.2–0.4% into the inner 80% of the unablated shell in ignition DT implosions at an incident intensity of 10^{15} W/cm^2. Preheat mitigation using a mid-Z Si layer in the ablator can reduce the preheat by an additional factor of 2 to ∼0.1–0.2%, making it close to 0.15% of the laser energy, which is the acceptable level of preheat for present ignition direct-drive designs [20]. Note that improved beam smoothing can further reduce LPI; it has been found on OMEGA to reduce hot-electron production by ∼20% [30,32].

In conclusion, hot-electron preheat and energy deposition has been studied in the PDD experiments on the NIF. Hot-electron coupling from 0.2% to 0.4% of the laser energy to the unablated shell is inferred when the incident laser intensity increases from 0.75×10^{15} to 1×10^{15} W/cm^2, with half of the preheat coupled to the inner 80% of the unablated shell. The use of mid-Z Si layers strategically placed in the ablator has been shown to reduce the preheat by about a factor of ∼2 at an incident intensity of 10^{15} W/cm^2. This provides a promising preheat-mitigation strategy that can expand the ignition-design space to higher intensity. Preheat extrapolation to ignition-scale cryogenic DT implosions on the NIF shows that preheat levels can be acceptable for on-target intensities close to 10^{15} W/cm^2.

ACKNOWLEDGMENTS

This material is based upon work supported by the Department of Energy National Nuclear Security Administration under Award No. DE-NA0003856, the University of Rochester, and the New York State Energy Research and Development Authority. The support of the U.S. Department of Energy does not constitute an endorsement by the U.S. DOE of the views expressed in this paper. This report was prepared as an account of work sponsored by an agency of the U.S. Government. Neither the U.S. Government nor any agency thereof, nor any of their employees, makes any warranty, express or implied, or assumes any legal liability or responsibility for the accuracy, completeness, or usefulness of any information, apparatus, product, or process disclosed, or represents that its use would not infringe privately owned rights. Reference herein to any specific commercial product, process, or service by trade name, trademark, manufacturer, or otherwise does not necessarily constitute or imply its endorsement, recommendation, or favoring by the U.S. Government or any agency thereof. The views and opinions of the authors expressed herein do not necessarily state or reflect those of the U.S. Government or any agency thereof.

[1] J. Nuckolls, L. Wood, A. Thiessen, and G. Zimmerman, Nature (London) **239**, 139 (1972).

[2] R. S. Craxton, K. S. Anderson, T. R. Boehly, V. N. Goncharov, D. R. Harding, J. P. Knauer, R. L. McCrory, P. W. McKenty, D. D. Meyerhofer, J. F. Myatt *et al.*, Phys. Plasmas **22**, 110501 (2015).

[3] W. Seka, E. A. Williams, R. S. Craxton, L. M. Goldman, R. W. Short, and K. Tanaka, Phys. Fluids **27**, 2181 (1984).

[4] H. Figueroa, C. Joshi, H. Azechi, N. A. Ebrahim, and K. Estabrook, Phys. Fluids **27**, 1887 (1984).

[5] C. S. Liu, M. N. Rosenbluth, and R. B. White, Phys. Fluids **17**, 1211 (1974).

[6] E. M. Campbell and W. J. Hogan, Plasma Phys. Controlled Fusion **41**, B39 (1999); G. H. Miller, E. I. Moses, and C. R. Wuest, Opt. Eng. **43**, 2841 (2004).

[7] M. J. Rosenberg, A. A. Solodov, J. F. Myatt, W. Seka, P. Michel, M. Hohenberger, R. W. Short, R. Epstein, S. P.

Regan, E. M. Campbell *et al.*, Phys. Rev. Lett. **120**, 055001 (2018).

[8] A. A. Solodov, M. J. Rosenberg, W. Seka, J. F. Myatt, M. Hohenberger, R. Epstein, C. Stoeckl, R. W. Short, S. P. Regan, P. Michel *et al.*, Phys. Plasmas **27**, 052706 (2020).

[9] M. J. Rosenberg, A. A. Solodov, W. Seka, R. K. Follett, J. F. Myatt, A. V. Maximov, C. Ren, S. Cao, P. Michel, M. Hohenberger *et al.*, Phys. Plasmas **27**, 042705 (2020).

[10] A. Simon, R. W. Short, E. A. Williams, and T. Dewandre, Phys. Fluids **26**, 3107 (1983).

[11] W. Seka, B. B. Afeyan, R. Boni, L. M. Goldman, R. W. Short, K. Tanaka, and T. W. Johnston, Phys. Fluids **28**, 2570 (1985).

[12] C. Stoeckl, R. E. Bahr, B. Yaakobi, W. Seka, S. P. Regan, R. S. Craxton, J. A. Delettrez, R. W. Short, J. Myatt, A. V. Maximov, and H. Baldis, Phys. Rev. Lett. **90**, 235002 (2003).

[13] W. Seka, D. H. Edgell, J. F. Myatt, A. V. Maximov, R. W. Short, V. N. Goncharov, and H. A. Baldis, Phys. Plasmas **16**, 052701 (2009).

[14] D. T. Michel, A. V. Maximov, R. W. Short, J. A. Delettrez, D. Edgell, S. X. Hu, I. V. Igumenshchev, J. F. Myatt, A. A. Solodov, C. Stoeckl *et al.*, Phys. Plasmas **20**, 055703 (2013).

[15] R. K. Follett, J. A. Delettrez, D. H. Edgell, V. N. Goncharov, R. J. Henchen, J. Katz, D. T. Michel, J. F. Myatt, J. Shaw, A. A. Solodov *et al.*, Phys. Rev. Lett. **116**, 155002 (2016).

[16] R. E. Turner, K. Estabrook, R. L. Kauffman, D. R. Bach, R. P. Drake, D. W. Phillion, B. F. Lasinski, E. M. Campbell, W. L. Kruer, and E. A. Williams, Phys. Rev. Lett. **54**, 189 (1985); J. R. Fein, J. P. Holloway, M. R. Trantham, P. A. Keiter, D. H. Edgell, D. H. Froula, D. Haberberger, Y. Frank, M. Fraenkel, E. Raicher *et al.*, Phys. Plasmas **24**, 032707 (2017); R. K. Kirkwood, B. J. MacGowan, D. S. Montgomery, B. B. Afeyan, W. L. Kruer, J. D. Moody, K. G. Estabrook, C. A. Back, S. H. Glenzer, M. A. Blain *et al.*, Phys. Rev. Lett. **77**, 2706 (1996); J. F. Myatt, H. X. Vu, D. F. DuBois, D. A. Russell, J. Zhang, R. W. Short, and A. V. Maximov, Phys. Plasmas **20**, 052705 (2013).

[17] S. Skupsky, J. A. Marozas, R. S. Craxton, R. Betti, T. J. B. Collins, J. A. Delettrez, V. N. Goncharov, P. W. McKenty, P. B. Radha, T. R. Boehly *et al.*, Phys. Plasmas **11**, 2763 (2004).

[18] T. J. B. Collins, J. A. Marozas, K. S. Anderson, R. Betti, R. S. Craxton, J. A. Delettrez, V. N. Goncharov, D. R. Harding, F. J. Marshall, R. L. McCrory *et al.*, Phys. Plasmas **19**, 056308 (2012); T. J. B. Collins and J. A. Marozas, *ibid.* **25**, 072706 (2018).

[19] M. Hohenberger, P. B. Radha, J. F. Myatt, S. LePape, J. A. Marozas, F. J. Marshall, D. T. Michel, S. P. Regan, W. Seka, A. Shvydky *et al.*, Phys. Plasmas **22**, 056308 (2015).

[20] J. A. Delettrez, T. J. B. Collins, and C. Ye, Phys. Plasmas **26**, 062705 (2019).

[21] M. Hohenberger, F. Albert, N. E. Palmer, J. J. Lee, T. Döppner, L. Divol, E. L. Dewald, B. Bachmann, A. G. MacPhee, G. LaCaille *et al.*, Rev. Sci. Instrum. **85**, 11D501 (2014).

[22] A. R. Christopherson, R. Betti, C. J. Forrest, J. Howard, W. Theobald, J. A. Delettrez, M. J. Rosenberg, A. A. Solodov, C. Stoeckl, D. Patel *et al.*, Phys. Rev. Lett. **127**, 055001 (2021).

[23] J. Delettrez, R. Epstein, M. C. Richardson, P. A. Jaanimagi, and B. L. Henke, Phys. Rev. A **36**, 3926 (1987).

[24] P. B. Radha, V. N. Goncharov, T. J. B. Collins, J. A. Delettrez, Y. Elbaz, V. Y. Glebov, R. L. Keck, D. E. Keller, J. P. Knauer, J. A. Marozas *et al.*, Phys. Plasmas **12**, 032702 (2005).

[25] The lower-wavelength limit of the SRS scattered light corresponds to the Landau dumping cutoff of the resonant plasma waves. The gap in SRS reflectivity between the underdense and $n_c/4$ features, frequently observed in experiments, is not well understood and several potential mechanisms were proposed in the past [33].

[26] S. Agostinelli, J. Allison, K. Amako, J. Apostolakis, H. Araujo, P. Arce, M. Asai, D. Axen, S. Banerjee, G. Barrand *et al.*, Nucl. Instrum. Methods Phys. Res., Sect. A **506**, 250 (2003).

[27] Target charge and electron recirculation by the electrostatic sheath fields can be reduced by a return current through the stalk holding the target, set up by an electrical breakdown of the stalk material [34]. The role of the self-generated quasistatic magnetic fields in the coronal plasma [35] and their effect on hot-electron transport is not fully understood.

[28] J. D. Moody, P. Datte, K. Krauter, E. Bond, P. A. Michel, S. H. Glenzer, L. Divol, C. Niemann, L. Suter, N. Meezan *et al.*, Rev. Sci. Instrum. **81**, 10D921 (2010).

[29] V. N. Goncharov, T. C. Sangster, R. Betti, T. R. Boehly, M. J. Bonino, T. J. B. Collins, R. S. Craxton, J. A. Delettrez, D. H. Edgell, R. Epstein *et al.*, Phys. Plasmas **21**, 056315 (2014).

[30] M. J. Rosenberg, A. A. Solodov, P. B. Radha, W. Theobald, C. Stoeckl, V. Y. Glebov, C. Forrest, D. Edgell, R. Betti, A. R. Christopherson *et al.*, Hot electron preheat in hydrodynamically scaled direct-drive inertial confinement fusion implosions on the NIF and OMEGA (unpublished).

[31] R. Betti, V. Gopalaswamy, A. Lees, D. Patel, and J. Knauer, Exploring pathways to hydro-equivalent ignition on the OMEGA laser, presented at the 62nd Annual American Physical Society Division of Plasma Physics Meeting, remote, 9–13 November 2020.

[32] D. Turnbull, A. V. Maximov, D. Cao, A. R. Christopherson, D. H. Edgell, R. K. Follett, V. Gopalaswamy, J. P. Knauer, J. P. Palastro, A. Shvydky *et al.*, Phys. Plasmas **27**, 102710 (2020).

[33] W. Rozmus, R. P. Sharma, J. C. Samson, and W. Tighe, Phys. Fluids **30**, 2181 (1987); H. C. Barr, T. J. M. Boyd, and A. P. Mackwood, Phys. Plasmas **1**, 993 (1994); H. A. Rose and P. Mounaix, *ibid.* **18**, 042109 (2011).

[34] N. Sinenian, M. J.-E. Manuel, J. A. Frenje, F. H. Séguin, C. K. Li, and R. D. Petrasso, Plasma Phys. Control. Fusion **55**, 045001 (2013).

[35] F. H. Séguin, C. K. Li, M. J.-E. Manuel, H. G. Rinderknecht, N. Sinenian, J. A. Frenje, J. R. Rygg, D. G. Hicks, R. D. Petrasso, J. Delettrez *et al.*, Phys. Plasmas **19**, 012701 (2012).